Supporting Information

From muscle to motion: GaIn nanoparticle-TPU core/shell mesh electrodes for intelligent prosthesis

Yeonjee Jeon[a]†, Seongjun Moon[a]†, Chanho Jung[a], Jonghyeon Noh[a], Jaeyu Lee[b], Safina Abdusamievna Saidova[c], Jaehun Lee[a], Seungseok Han[a], Seonju Jeong[a], Kee-Eung Kim[d], Wu Bin Ying[a], Kyung Jin Lee[b]*, and Jung-Yong Lee[a]**

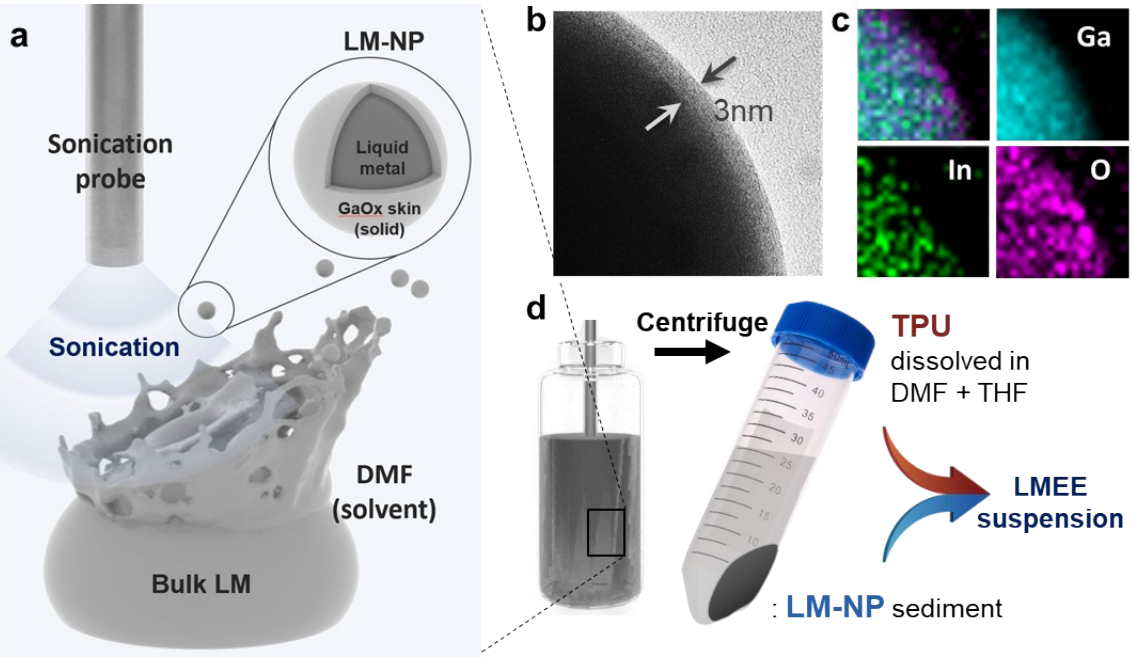

Figure S1. **Preparation of LMEE suspension for electrode fabrication.** (**a**) Schematic of the sonication process used to disperse liquid metal in DMF and THF. (**b**) TEM image showing gallium oxide shells formed around LM-NPs after sonication. (**c**) EDS mapping image of LM-NPs indicating the presence of Ga (blue), In (green), and oxygen (magenta). (**d**) Schematic of the centrifugation step for separating the denser LM-NP sediments.

The fabrication of the liquid metal embedded elastomer (LMEE) suspension begins with the sonication of eutectic gallium-indium (EGaIn), a liquid metal (LM), in N N-Dimethylformamide (DMF), as depicted in **Figure S1a**.[1, 2] Utilizing a probe sonicator, bulk LM is fragmented into nano-scaled particles, crucial for achieving a homogeneous dispersion. This foundational step ensures that the nanoparticles (NPs) are optimally prepared for subsequent encapsulation and application.

Following sonication, the transmission electron microscopy (TEM) image in **Figure S1b** reveals the formation of Ga oxide shells (thickness: ~ 3 nm) around the NPs. These shells provide stability and prevent aggregation. Energy-dispersive X-ray spectroscopy (EDS) mapping, displayed in **Figure S1c**, further delineates the elemental composition of the LM-NPs, highlighting the presence of Ga (blue), In (green), and oxygen (magenta). The core is primarily composed of an In-Ga alloy, encased within an oxygen-rich Ga oxide shell. The formation of this shell, driven by the oxygen from the sonication solvent, is essential for maintaining controlled conductivity that is pivotal for precise electrode fabrication through jetting techniques.

The process ends with a centrifugation step, as illustrated in **Figure S1d**, which separates the denser LM-NPs sediment. These sediments are subsequently dispersed in a mixed solvent of DMF, tetrahydrofuran (THF), and thermoplastic polyurethane (TPU) to create the conductive ink utilized in the charge-reverse electro writing (CREW) printing process. This rigorously controlled preparation process ensures the production of conductive inks that are critical for fabricating electrodes with enhanced precision and conductivity, pivotal for the progress of wearable electronic devices.

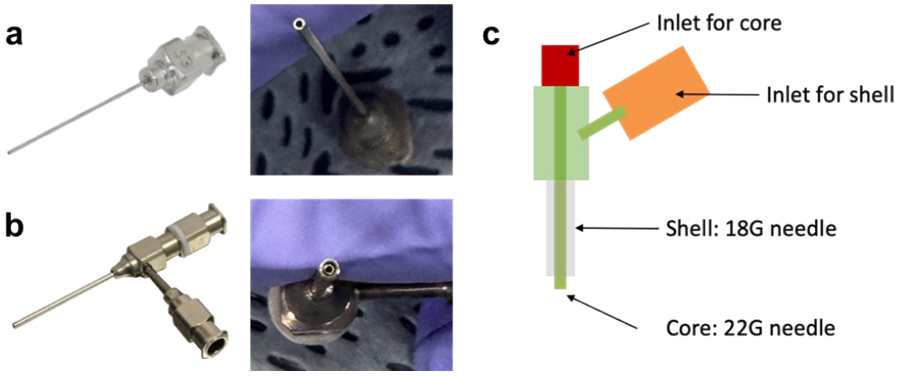

Figure S2. **Digital images** of (**a**) the needle and (**b**) the coaxial needle for preparing single phasic and core/shell microfiber, respectively. (**c**) Schematic diagram for the coaxial needle.

Figure S2a, **S2b** and **S2c** illustrate the needles used to fabricate single phasic and core/shell microfibers. 18G and 22 G needles were adopted for the shell and core, respectively. In addition, the behavior of the fluid can be analyzed from the Reynolds number (*Re*) using the following equation:

$$Re = \frac{u \cdot d}{v},$$

where u, d, and v denote the fluid velocity, internal diameter of the pipe, and kinematic viscosity, respectively.[3] Laminar flow occurs when $Re < 2300$ while turbulent flow occurs when $Re > 2900$.[4, 5] Hence, it can be inferred that a higher kinematic viscosity of the polymeric solution and slower fluid velocity both increase the probability of laminar flow. Given the conditions in our system, the *Re* values of the core-flow and shell-flow can be calculated as 1.46×10^{-11} and 7.18×10^{-12}, respectively, thus, implying that both flows maintain a laminar state.

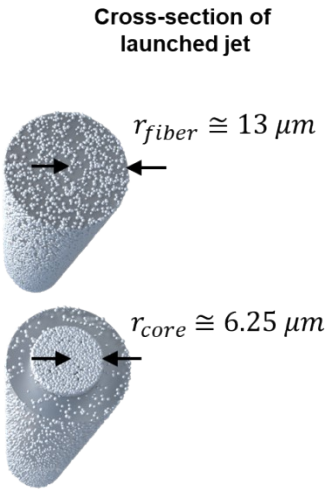

Figure S3. Schematic of jet launch and conductivity calculations.

Figure S3 depicts the cross-sectional view of the jet launched from the needle tip during the CREW process. The calculated conductivity values, shown in **Figure 1d**, demonstrate the precision required to achieve successful jetting within specified conductivity thresholds. Maintaining conductivity below the critical threshold of 1 µS/cm, a parameter experimentally validated in **Figure 1b**, is pivotal for avoiding sparking and preserving the jet's structural integrity during the printing process.

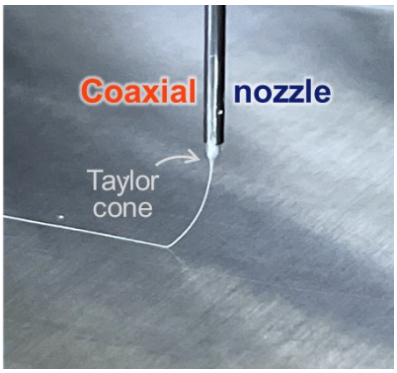

Figure S4. Visualization of the Taylor cone formation in core/shell micro-jet.

Figure S4 displays the Taylor cone formation at the tip of the coaxial nozzle during the jet launching process, a critical aspect of the CREW technique. The stable formation of the Taylor cone is achieved through meticulous control of the suspension's feeding rate, viscosity, and fluidity. These parameters are optimized to ensure a consistent laminar flow of the core/shell micro-jet, crucial for precise and defect-free fiber fabrication. This visualization highlights the effective integration of fluid dynamics and materials science to achieve controlled electrospinning.

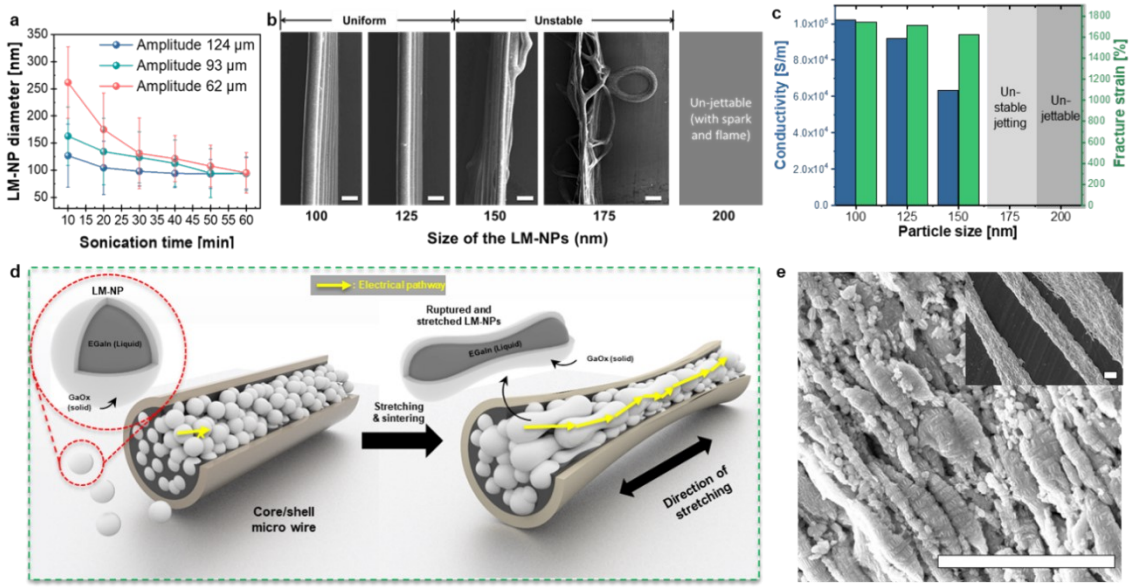

Figure S5. Influence of LM-NP Size on LMEE Microfiber Properties. (**a**) Sonication power and duration impact on LM-NP size distribution. (**b**) SEM images of formed LMEE microfibers incorporating LM-NPs of various sizes. Scale bars, 30 μm. (**c**) Resistance and fracture strain values of core/shell LMEE fibers depending on the size of LM-NPs in the core section. (**d**) Schematic of the sintering process of LMEE@TPU fiber. (**e**) SEM image of shell-uncovered singular microfiber after the stretching process. Scale bars, 5 μm.

We investigated the effect of sonication amplitude and duration on the size distribution of the LM-NPs (**Figure S5a**). The sizes of LM-NPs varied from 261.7 to 95.22 nm. After 40 minutes of sonication at the highest amplitude, the smallest particle size with a narrow standard deviation was achieved. However, the particle size converged to 100 nm after 60 minutes, regardless of the amplitude conditions. The selection of particle size is critical in the fabrication process because it deeply influences the electrical and mechanical properties of the microfiber and the processability of the electrospinning system.[6]

The conductivity of LMEE suspensions was investigated for various sizes of the LM-NPs. TPU was selected as an elastomer for the polymeric matrix because of its excellent stretchability. Mixtures containing 1 g of LM-NPs and 0.1 g of TPU (LMEE10) were dissolved in a solvent blend of THF and DMF. The suspension conductivities were measured at 1.43 μS/cm for 100 nm and 1.56 μS/cm for 200 nm LM-NPs, indicating that the conductivity increases with nanoparticle size.

Next, we applied various-sized LM-NPs (100–200 nm) into the jetting process (**Figure S5b**). As the particle size increased, the morphologies of the microfibers became unstable due to

heightened suspension conductivity. Specifically, suspensions containing 150 and 175 nm-sized LM-NPs exhibited unstable jetting characterized by whipping motions. Using LM-NPs larger than 200 nm resulted in severe discharging issues between the nozzle and collector, affirming that the smallest-size LM-NPs (100 nm) was the most suitable for stable jetting. Moreover, the impact of LM-NP size on the electromechanical properties of core/shell microfibers was assessed using the LMEE10@TPU configuration. Nanoparticles with diameters of 100, 125, 150, 175, and 200 nm were tested. Nanoparticles larger than 150 nm proved challenging to jet due to increased conductivity leading to discharging and sparking. The fracture strains of microfibers, depicted by green bars in **Figure S5c**, slightly increased as particle size decreased.[7] This trend is attributed to the easy agglomeration and close-packing of small-sized particles. In general, aggregates of small LM-NPs provide a larger specific surface area than larger LM-NPs of equivalent volume. However, the interstitial volume among small LM-NPs may be too limited for polymers to adequately fill, resulting in a reduced effective surface area. This, in turn, delays crack onset in microfibers composed of smaller LM-NPs.

Conductivity changes, represented by blue bars in **Figure S5c**, showed a decline as the size of LM-NPs within the core increased. As the LM-NP size within the core section enlarges, the conductivity of the microfiber decreases further from 1.02×10^6 to 6.32×10^4 S/m, as the external force can break the shell of larger LM-NPs more efficiently, creating fewer but more effective percolation pathways.[8] **Figure S5d** illustrates these percolation pathways formed within the core/shell structure, and **Figure S5e** demonstrates the successful formation of an electrical pathway. This pathway is created from mechanically sintered LM-NPs. After the application of THF and subsequent drying, the agglomerated LM pathways within the LMEE fibers are exposed as THF effectively separates the TPU from the LM-NPs, revealing the underlying conductive network.

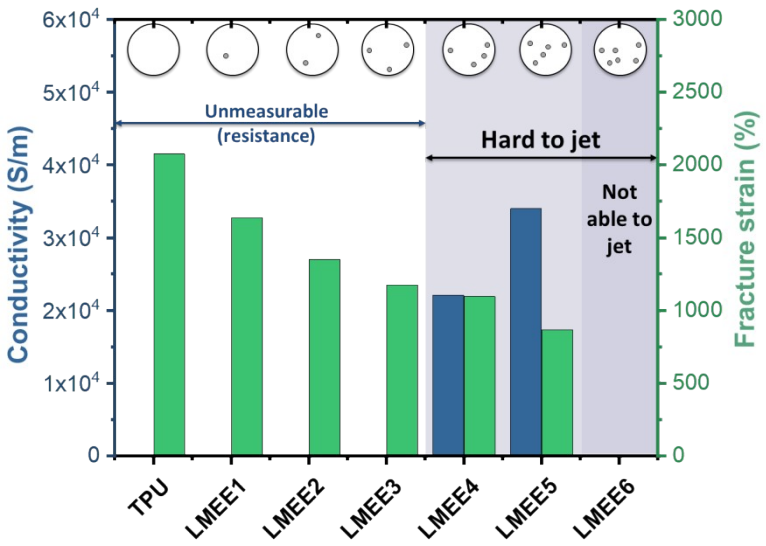

Figure S6. Maximum elongation and the conductivity of 40-stacked single-phasic microfiber for different weight ratios of LM-NPs to TPU.

Figure S6 presents the changes in the elongation at break and resistance depending on the weight ratio of LM-NPs in the single-phasic microfibers. As depicted in the figure, the elongation at break diminished with an increase in the weight ratio of LM-NPs in the structure. This effect is attributed to the increased number of LM-NPs leading to an increase in crack sites (**Figure S8**). The conductivity of the microfibers could only be reliably detected from LMEE4 and LMEE5. Below LMEE3 level, the percolation network of LM-NPs was not fully formed.

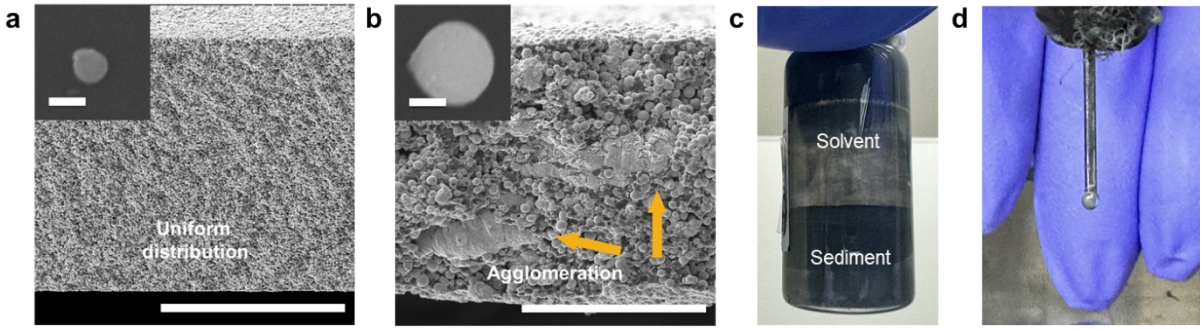

Figure S7. Digital images of composite films with different LM-NP sizes prepared via a casting method. Cross-sectional SEM images of the LMEE films with (**a**) 100-nm-sized lm-nps, and (**b**) 200-nm-sized LM-NPs. Scale bars, 100 μm. Insets represent SEM images of single particles, with scale bars, 100 nm. (**c**) Precipitation of LM-NPs in the LMEE suspension over time. (**d**) Nozzle blockage caused by precipitated particles.

The LM-NP size significantly influences their dispersion within the suspension and processability. With an increase in LM-NP size, their distribution within the solution becomes less uniform, leading to accumulation and eventual sedimentation in composite films. As shown in **Figure S7a**, smaller-sized LM-NPs resulted in a markedly uniform distribution in LMEE films, indicating that they are well-dispersed in the suspension. However, with larger LM-NPs, which are comparatively heavier and more fragile, sedimentation and sintering occur (**Figure S7b**), causing them to settle at the bottom and aggregate into bulk LM. Indeed, larger LM-NPs show sedimentation within an LMEE suspension (**Figure S7c**), often resulting in nozzle blockage, as shown in **Figure S7d**. These findings indicate that controlling the size of LM-NPs is crucial for maintaining a homogeneous dispersion within the suspension, which is essential for creating electrodes with uniform properties and maintaining their processability.

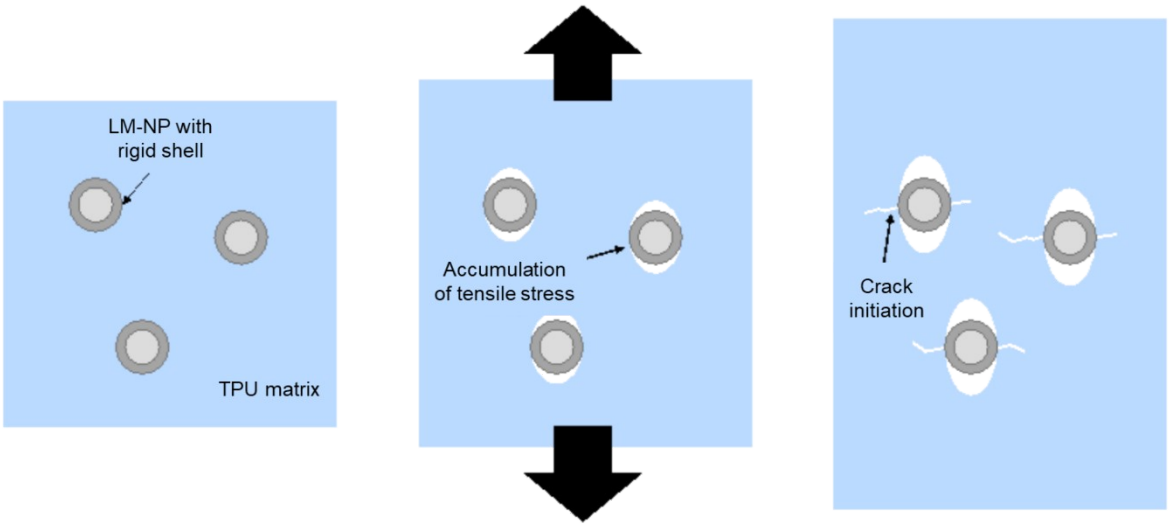

Figure S8. Schematic of crack onset by the introduction of LM-NPs in the composite matrix.

Figure S8 depicts a schematic of the crack-onset mechanism by the introduction of LM-NPs in the composite matrix. As the matrix was stretched by an external force, the interface between the LM-NPs and TPU matrix could be de-bonded, thereby generating a void because of the low interfacial affinity of LM-NPs and the TPU matrix. Then, as the matrix stretches, stress accumulates around the voids, leading to crack initiation.

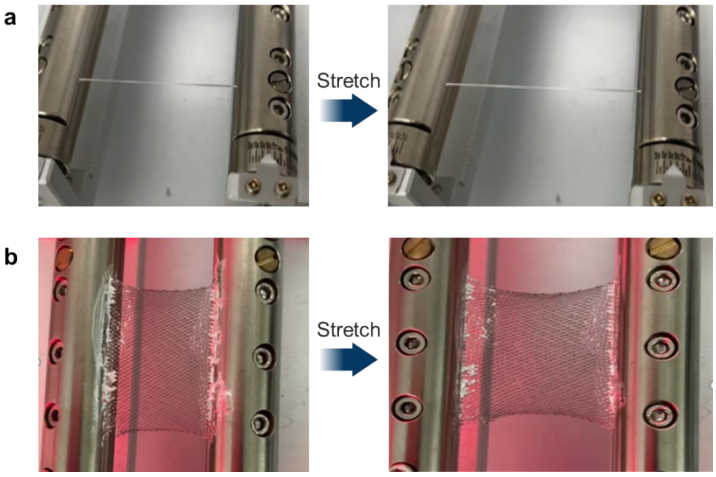

Figure S9. Digital images of tensile and cyclic testing process. (**a**) a single LMEE fiber, and (**b**) a mesh electrode with a scaffold-patterned structure.

Figure S9 presents images of a tensile test of electrodes before strain (left) and after stretching (right). The stretching was conducted at a speed of 0.1 mm/s and an acceleration of 0.01mm/s^2.

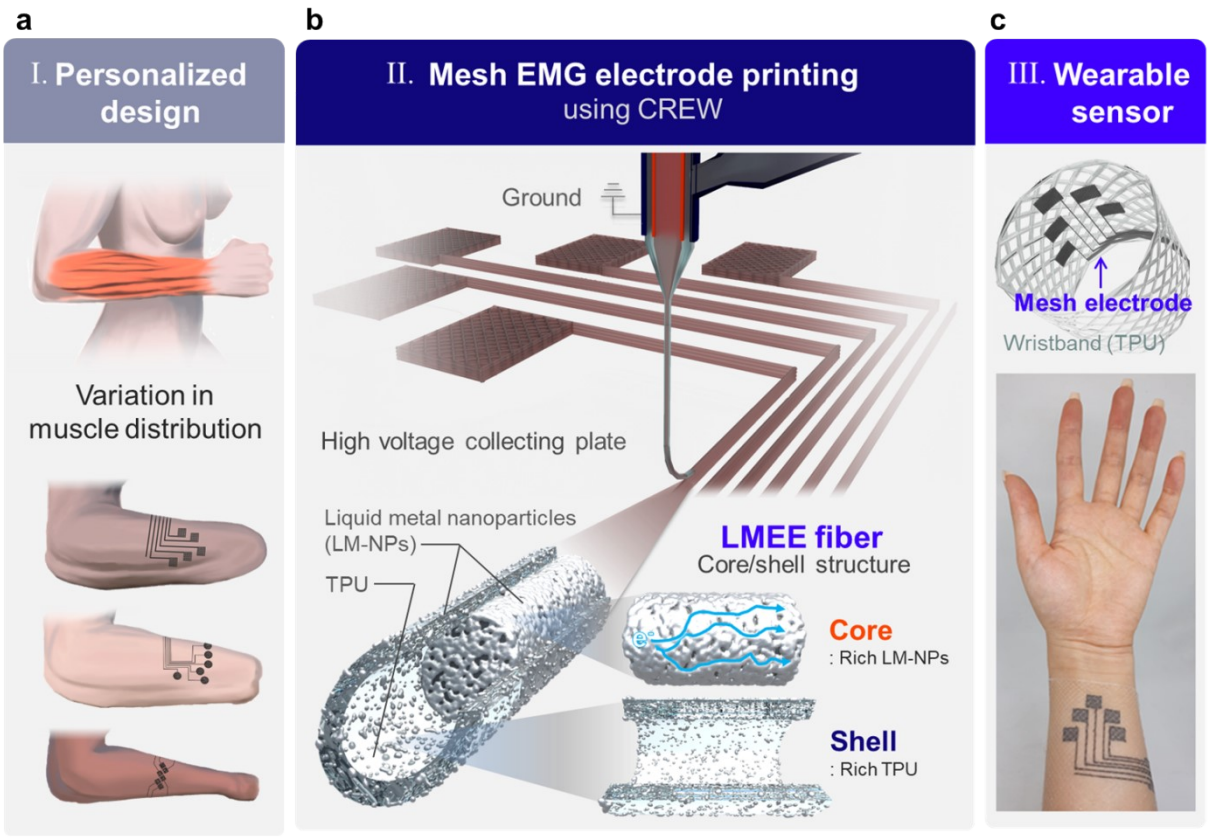

Figure S10. **Stages of EMG wristband fabrication using CREW technology.** (**a**) Schematic of the initial design phase, outlining the personalized EMG electrode pattern tailored to the user's muscle distribution to ensure optimal signal capture. (**b**) Diagram illustrating the application of the CREW technique for the accurate deposition of conductive ink. (**c**) Completed assembly of the EMG wristband integrated onto a stretchable TPU wristband, showcasing the electrode configuration and ease of use.

The EMG wristband fabrication involves two primary stages, beginning with the personalized design of the EMG electrode pattern, as shown in **Figure S10a**. This initial design is critical for aligning the electrodes according to the user's unique muscular structure, which significantly enhances signal accuracy and consistency. This is depicted in detail in **Figure S11**, illustrating the blueprint creation process. Unlike traditional bio-electrodes which require frequent repositioning, the mesh electrode wristband design necessitates only a one-time prefabrication measurement, ensuring consistent alignment and reusability.

The second stage employs the CREW method to accurately pattern the conductive ink comprising a LMEE suspension, formed by sonication of bulk LM into nano-sized particles and embedding them within a TPU matrix. This process, shown in **Figure S10b**, stabilizes the ejected jets to form fibrous structures under 20 micrometers thick, which is critical for

achieving high resolution in wearable electrode applications. By employing a coaxial nozzle setup, the wristband incorporates an LM-NPs-rich core for enhanced conductivity, encased within a TPU-rich shell for increased mechanical robustness.

The final product, as depicted in **Figure S10c** and **Figure S12**, is a wristband fully composed of TPU, ensuring wearability and ease of use. This design facilitates easy fastening and removal of the wristband, supporting daily usability and comfort.

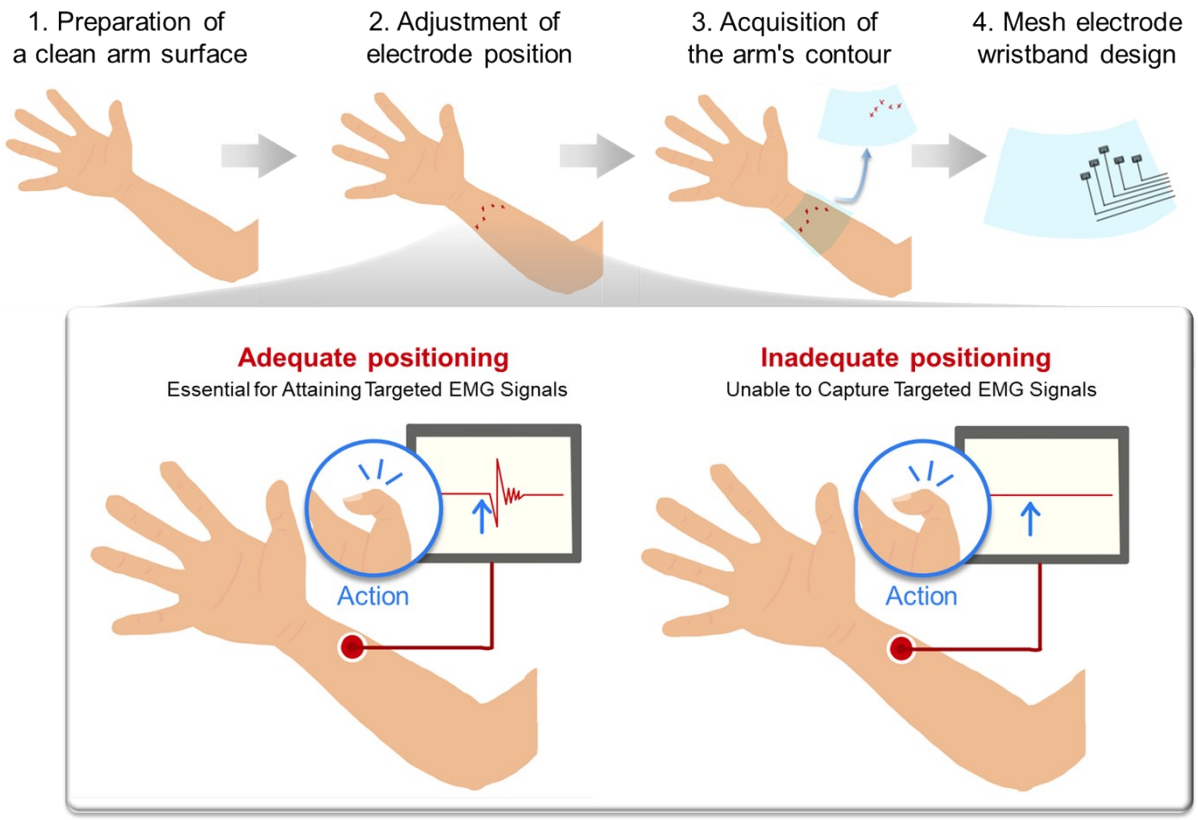

Figure S11. Design workflow of a custom-fit EMG wristband with mesh electrodes, tailored to conform to the unique muscle distribution of an individual.

Figure S11 outlines the critical steps necessary for determining the most effective placement of EMG electrodes to capture accurate muscle signals. The process begins with the preparation of the arm, which includes cleaning with alcohol and optional hair removal for better electrode-to-skin contact. Next, the electrode is positioned to pinpoint the site where the strongest desired signal is detected. This optimal location is identified through continuous monitoring and adjustment while evaluating signal quality. Once the ideal electrode site is established, the unique contours of the arm are mapped with special attention to the marked electrode positions. The final step involves designing the EMG wristband, integrating the electrodes, reference and connection ports according to the arm's profile and the optimal signal locations.

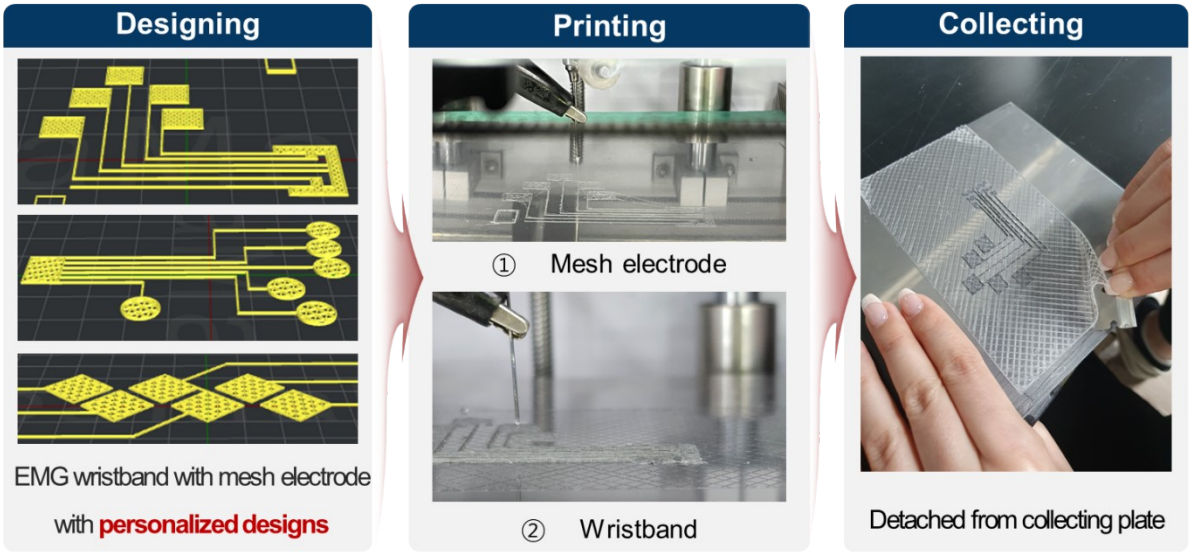

Figure S12. Fabrication process of an EMG wristband with mesh electrode.

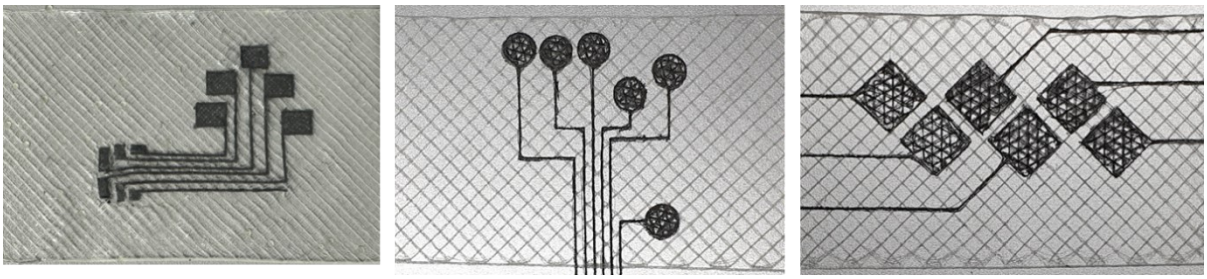

Figure S13. Various EMG wristbands with mesh electrode designs.

Figure S13 illustrates the various designs of the EMG wristband with mesh electrodes. The designed electrode pattern (**Figure S12**) was printed using the CREW technique. Subsequently, a TPU wristband was printed and adjoined onto the patterned mesh electrode. Lastly, the mesh electrode wristband that consists of patterned mesh electrodes and the TPU wristband were carefully removed from the collecting plate. **Figure S13** also shows various mesh electrode wristband designs tailored to an individual's muscle distribution.

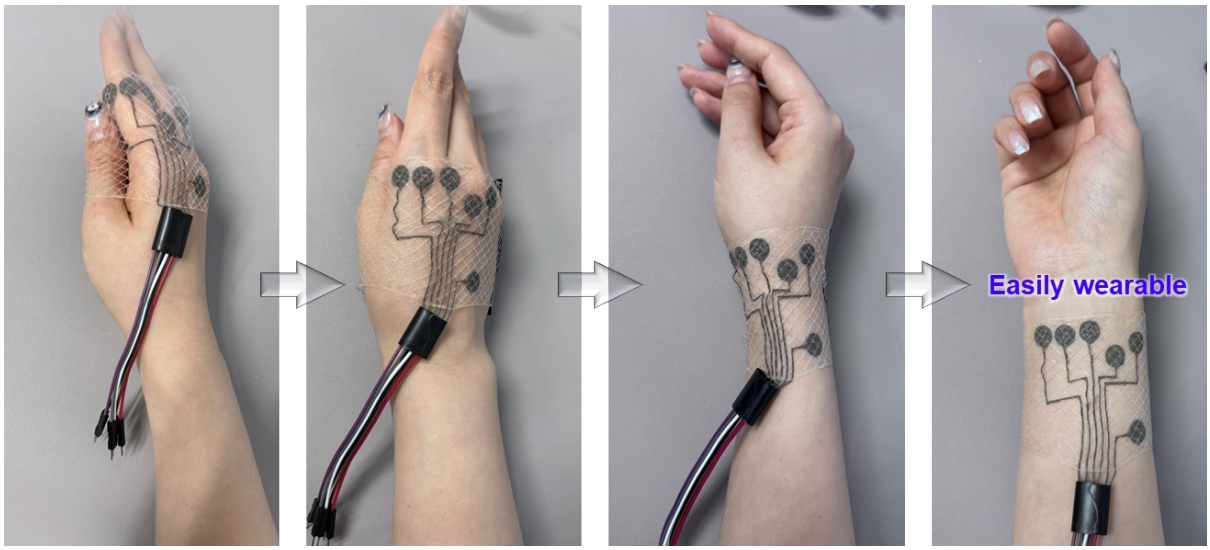

Figure S14. User-friendly EMG wristband with mesh electrodes.

Figure S14 illustrates the simple process of wearing the EMG wristband. Designed with elasticity, the wristband can be worn as effortlessly as a regular wristband accessory.

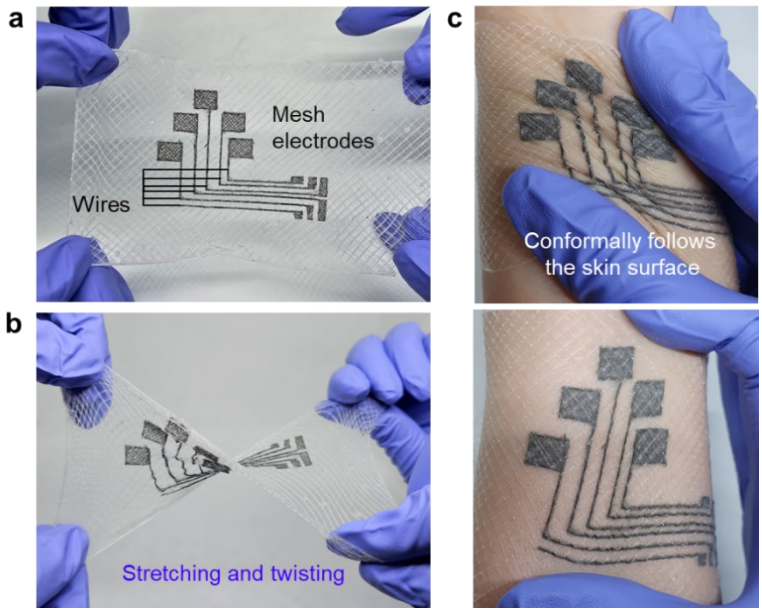

Figure S15. **Design and functionality of the EMG electrode wristband.** (**a**) Overview of the EMG wristband. (**b**) Demonstration of the wristband's omnidirectional stretchability, facilitated by the intrinsic properties of LMEE and TPU, which enable the wristband to conform to natural body contours without compromising functionality. (**c**) Close-up view showing the seamless integration between the mesh electrodes and the skin.

Figure S15a illustrates the EMG electrode wristband, which comprises five primary mesh electrodes for detecting EMG signals, smaller mesh electrodes for external connectivity, and connecting wires mounted on a TPU wristband. The primary mesh electrodes were designed to capture the EMG signals associated with the movements of each finger. An extra wire electrode functions as a reference electrode.

This aspect has significant potential in terms of aesthetics, as the mesh electrode can be customized to reflect individual preferences, as depicted in **Figure S13**. The intrinsic stretchability of both LMEE and TPU enables the wristband embedded with the mesh electrodes to stretch and twist in all directions (**Figure S15b**). The flexibility and omni-stretchability are crucial for the EMG electrode, as it must adhere smoothly to the skin to accurately record the bio-signal. Unlike commonly used electrolyte electrodes, which require adhesive for proper skin attachment due to insufficient stretchability (**Figure S16**), our EMG wristband with mesh electrodes conforms to the skin surface. This elasticity, provided by the TPU, enhances superior electrical contact between the skin and electrodes, as depicted in **Figure S15c**.

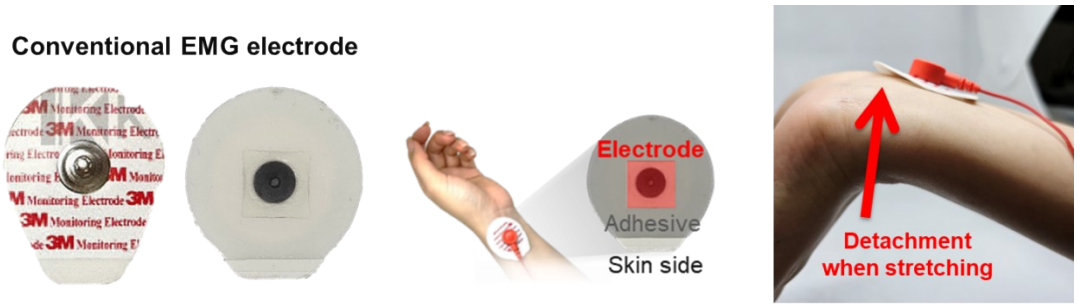

Figure S16. Digital images of conventional Ag/AgCl gel patches.

Figure S16 shows the commercially available 3M monitoring electrodes that are commonly employed for reading bio-electrical signals. These electrodes typically consist of an Ag/AgCl electrolyte gel patch, which is key for effective signal detection, and are backed with foam tape for improved skin contact. However, under stretching conditions, these electrodes often experience detachment from the skin, resulting in difficulties in obtaining reliable EMG signals.

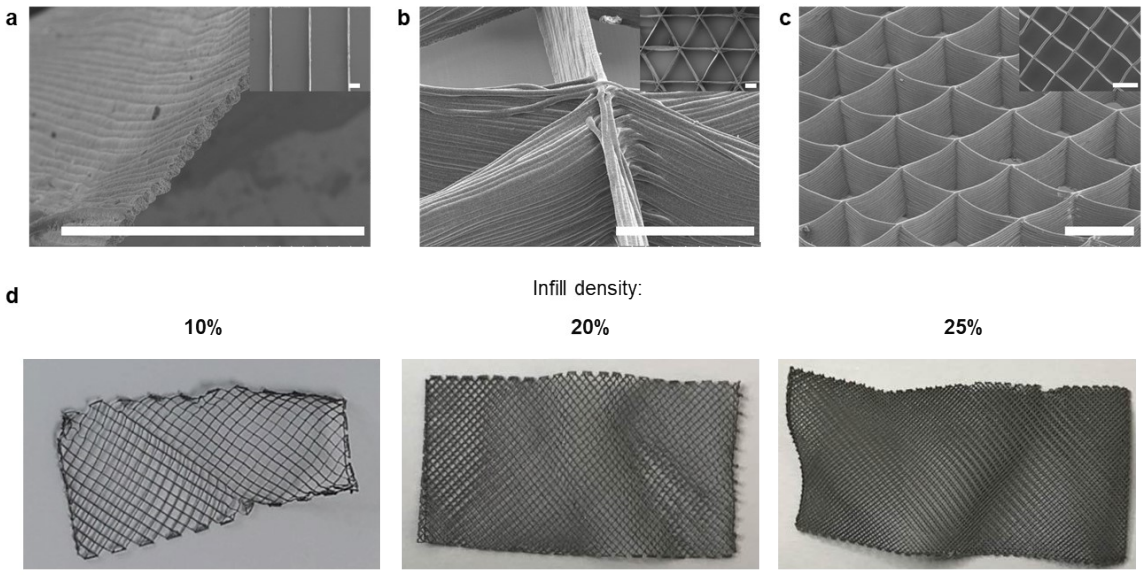

Figure S17. Diverse structures of mesh electrode fiber using CREW and 3D patterns. (**a**)-(**c**) SEM images of various structures of mesh electrode fiber through CREW process. (**d**) Digital images of the mesh electrodes with different infill densities.

Figure S17 presents a 3D scaffold patterns, illustrating the capabilities of a 3D printing machine in precision fabrication and the SEM images of the resulting structures (**a** linear, **b** triangular, and **c** rectangular). The printer follows the pre-designed and sliced 3D pattern using the ideaMaker software, allowing for fine control over the density of the scaffold and the spacing between the LMEE microfibers (**Figure S17d**).

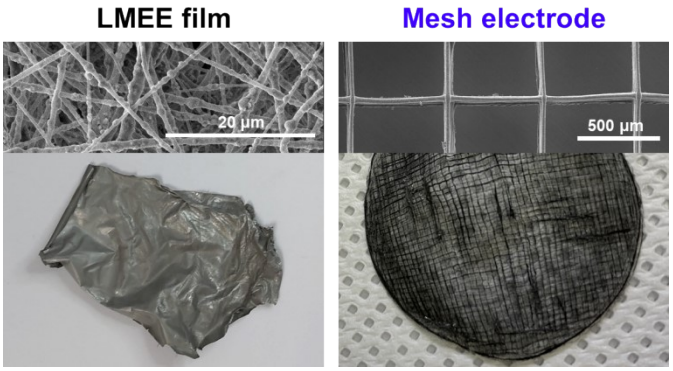

Figure S18. Comparison of non-woven LMEE film (left) and scaffold-patterned mesh electrode (right) for WVTR and SVTR.

Figure S18 illustrates a non-woven LMEE film fabricated via electrospinning and a mesh electrode fabricated using the CREW technique. Both were prepared to compare their water vapor transmission rate (WVTR) and sweat vapor transmission rate (SVTR). The non-woven LMEE film has a controlled thickness of approximately 80 μm, while the mesh electrode measures 200 μm in thickness. The SEM image of the LMEE film reveals a random alignment of LMEE fibers, resulting from the whipping behavior during the electrospinning process.

Figure S19. Demonstration of a data glove with integrated flexible strain sensors.

Figure S19 shows a data glove with embedded flexible strain sensors. These sensors detect bending movements of the fingers by monitoring changes in electrical resistance through an Arduino microcontroller.

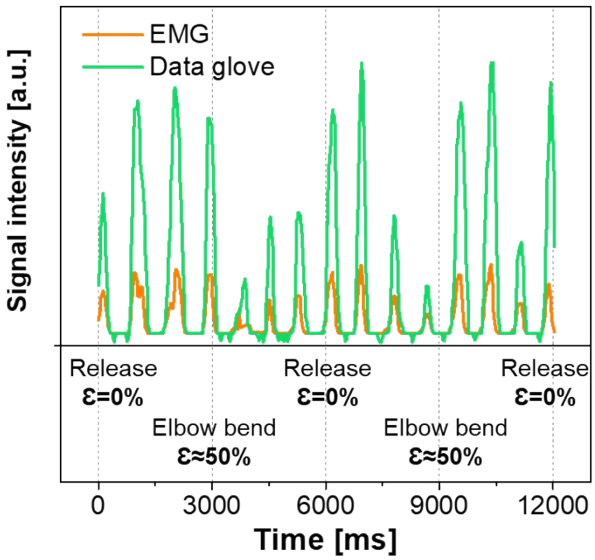

Figure S20. EMG–dataglove correlation of an aged mesh electrode wristband (after 100 stretch cycles and a year of air storage) during cyclic elbow flexion–extension (3 s per motion).

To evaluate real-world motion stability and durability, we performed additional EMG-reading tests using a mesh-electrode wristband that had undergone more than 100 cyclic stretching operations and had been stored in ambient air for over one year prior to measurement. During experiments involving repeated elbow flexion–extension movements at 3 s intervals (6 s per cycle) and middle-finger bending–release motions, the EMG signals obtained from the mesh electrode showed a highly consistent temporal trend with those from the dataglove reference. Quantitatively, the HSIC value between the two datasets was 0.032, which is statistically indistinguishable from the previously reported value for the freshly prepared mesh electrode (HSIC = 0.0359 ± 0.004, **figure 5d**).

This result demonstrates that even after prolonged storage and multiple mechanical cycles, the LMEE wristband maintains stable electrical performance and reliable signal decoding under dynamic body movements. The preserved correlation with the ground-truth glove data verifies both the mechanical robustness and long-term functional durability of the electrode during cyclic deformation.

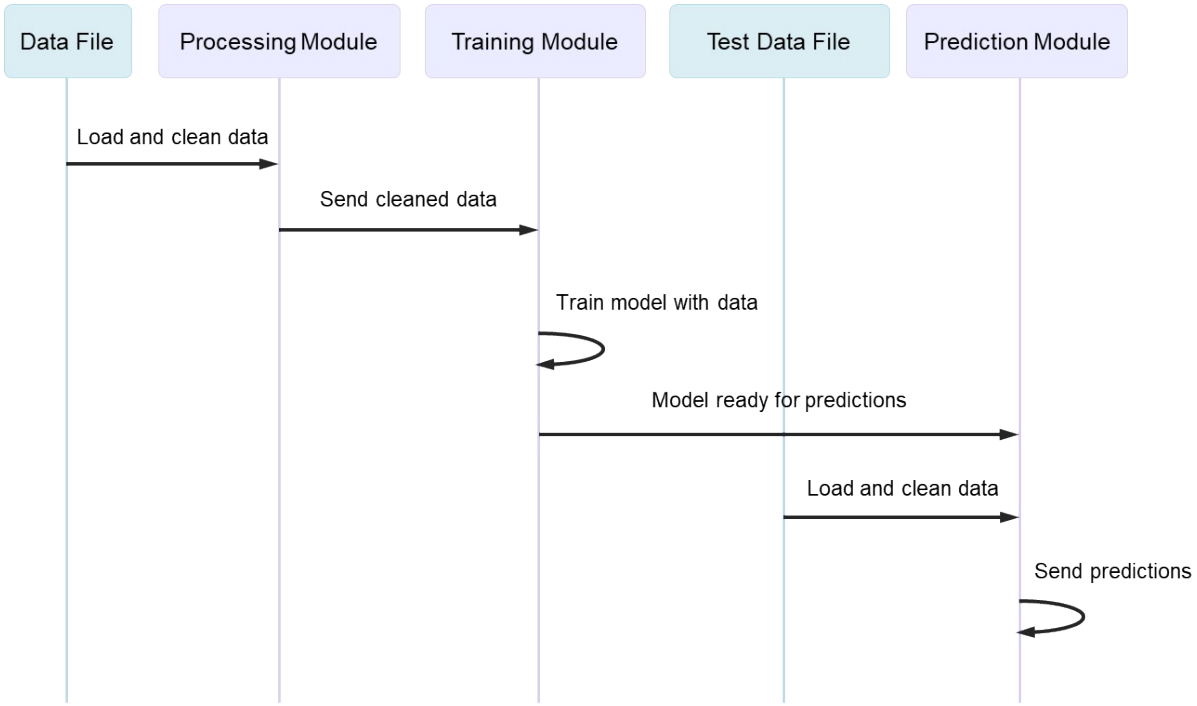

Figure S21. Sequential diagram of EMG signal processing and prediction using a multi-layer perceptron (MLP).

Figure S21 illustrates the comprehensive workflow for processing raw input data, including EMG signals and corresponding dataglove outputs that track finger movements, stored in the 'Data File'. This data is first refined in the 'Preprocessing Module' to ensure consistency and quality before being used to train a sophisticated MLP within the 'Training Module'. The MLP, chosen for its robust pattern recognition capabilities, is ideally suited for correlating EMG signals with precise finger movements. Following successful training, as indicated by a feedback loop in the 'Training Module', the MLP—configured with a hidden layer of 20 neurons—is ready to predict and control finger movements based on new EMG inputs. The training phase involves iterative adjustments and validations to optimize the model's performance. In the 'Prediction Module', the MLP analyzes cleaned test data from a separate 'Test Data File' to generate accurate predictions for prosthetic control. The process effectively transforms EMG signals, characterized by various jagged waveforms including those with multiple peaks within a single movement, into smoother waveforms that are better suited for controlling robotic prosthetic limbs.

Table S1. Composition of LM-NPs embedded elastomer suspensions.

Sample name	Weight of LM-NP (g)	Weight of TPU (g)	Volume of THF (mL)	Volume of DMF (mL)
TPU only	0	2	6	4
LMEE1	1	1	3	2
LMEE2	2	1	3	2
LMEE3	3	1	3	2
LMEE4	4	1	3	2
LMEE5	5	1	3	2
LMEE6	6	1	3	2
LMEE7	7	1	3	2
LMEE8	8	1	3	2
LMEE9	9	1	3	2
LMEE10	10	1	3	2

Table S2. Comparative conductivity and SNR values across various wearable electrode studies.

Conductivity (S/m)	**SNR (dB)**	**Ref.**
2.50×10^{0}	2.5	[9]
7.00×10^{5}	3.2	[10]
4.56×10^{3}	24.1	[11]
1.31×10^{4}	35.2	[12]
5.00×10^{1}	9.4	[13]
1.96×10^{0}	30.8	[14]
7.14×10^{0}	28.9	[15]
1.83×10^{0}	29.3	[16]
2.20×10^{4}	20.0	[17]
1.12×10^{0}	28.3	[18]
2.84×10^{0}	24.8	[19]
3.00×10^{3}	1.4	[20]
9.87×10^{3}	24.3	[21]

2.80×10^{-3}	15.9	[22]
2.50×10^{5}	20.3	[23]
2.64×10^{5}	30.0	**This work**

Table S3. **Comparative gauge factor and fracture strain across various wearable electrode studies.**

Gauge factor	Fracture strain (%)	Ref.
8.38×10^{-1}	100	[24]
6.59×10^{2}	520	[25]
1.52×10^{0}	450	[26]
9.60×10^{-1}	50	[27]
1.00×10^{0}	1425	[16]
6.90×10^{2}	40	[28]
1.73×10^{0}	370	[29]
2.00×10^{1}	450	[30]
1.16×10^{1}	795	[31]
1.42×10^{1}	880	[32]
1.70×10^{1}	85	[33]
5.50×10^{3}	1600	[17]
4.70×10^{0}	2400	[18]
6.90×10^{-1}	1898	[34]
1.01×10^{1}	400	[35]
9.80×10^{-2}	866	**This work**

Movie 1

Movie 1 illustrates the overall concept of this study, presenting the complete workflow from material design to functional demonstration. The video sequentially shows the charge-reverse electro-writing (CREW) process used to fabricate the liquid-metal–elastomer (LMEE) mesh electrodes, the formation of core/shell microfibers, and their integration into a flexible EMG

wristband. It then visualizes how the wristband captures muscle signals during motion and how these signals are decoded via a machine-learning model to control a robotic prosthetic hand in real time, highlighting the system's user-friendly operation and practical applicability.

Movie 2.

This video captures a real-time performance comparison between Ag/AgCl electrodes and our EMG wristband, when applied under various mechanical strain conditions to a human arm. It specifically illustrates the EMG wristband's responsiveness during a thumbs-down gesture, demonstrating its superior stability and sensitivity under dynamic conditions.

Movie 3.

Demonstrating the limitations of simple threshold-based EMG signal processing for robotic arm control, this video highlights the enhancements in prosthetic responsiveness achieved through machine learning integration. It features a MLP processing both EMG signals and dataglove inputs, illustrating the robotic arm's improved ability to mimic natural human finger movements with high accuracy and responsiveness.

Appendix 1: The running cods of signal processing codes using MLP

```
import numpy as np
import pandas as pd

w_size = 10

file_name = 'Micro_wires_v36_signal_processing.xlsx'  # 실제 파일 경로로 대체
data_df = pd.read_excel(file_name, sheet_name='Data')
data_df = data_df.iloc[3:,2:]
data_df.dropna(inplace=True)
display(data_df)

import itertools

electrode_type = ['conventional', 'ccfe']
finger = ['thumb', 'index', 'middle', 'ring', 'little']
under = ['no_strain', 'strain']
source = ['electrode', 'dataglove']
column_names = [f'{e}_{f}_{u}_{s}' for e,f,u,s in itertools.product(electrode_type,
finger, under, source)]
data_df.columns = column_names
display(data_df)
from sklearn.model_selection import train_test_split
from sklearn.pipeline import Pipeline
from sklearn.linear_model import LinearRegression
from sklearn.svm import SVR
from sklearn.neural_network import MLPRegressor
from sklearn.preprocessing import StandardScaler
from sklearn.metrics import mean_squared_error

def train_and_predict(input_column, output_column):
    X = data_df[[input_column]]
    Y = data_df[[output_column]]

    Y = Y.values.ravel()

    X_new = pd.concat([X.shift(i) for i in range(w_size)], axis=1)
    X_new.columns = [f'{X.columns[0]}_{i}' for i in range(w_size)]
```

```
    nan_rows = X_new.isna().any(axis=1)
    X_new = X_new[~nan_rows]
    Y_new = Y[~nan_rows]

    X_train, X_test, Y_train, Y_test = train_test_split(X_new.values, Y_new,
test_size=0.2, random_state=42)

    model = Pipeline([
        ('scaler', StandardScaler()),
        ('mlp', MLPRegressor(hidden_layer_sizes=(20,), activation='tanh',
max_iter=10000, learning_rate_init=0.05))
    ])
    model.fit(X_train, Y_train)



    mse = model.score(X_test, Y_test)
    print(f'MSE for {input_column} to {output_column}: {mse}')

        return model
# pairs = [('B', 'C'), ('D', 'E'), ('F', 'G'), ('H', 'I'), ('J', 'K'),
#          ('L', 'M'), ('N', 'O'), ('P', 'Q'), ('R', 'S'), ('T', 'U')]
# pairs = [('conventional_thumb_no_strain_electrode',
       'conventional_thumb_no_strain_dataglove')]

pairs = [('ccfe_little_no_strain_electrode', 'ccfe_little_no_strain_dataglove')]

models = {input_col: train_and_predict(input_col, output_col) for input_col,
output_col in pairs}

new_file_name = 'Micro_wires_v36_Test.xlsx'
df_test = pd.read_excel(new_file_name, sheet_name='Data')
X_test = df_test['A']
Y_test = df_test['B']

X_test_new = pd.concat([X_test.shift(i) for i in range(w_size)], axis=1)
X_test_new.columns = [f'x_{i}' for i in range(w_size)]

nan_rows = X_test_new.isna().any(axis=1)
X_test_new = X_test_new[~nan_rows]
```

```
Y_test_new = Y_test[~nan_rows]

Y_pred = models['ccfe_little_no_strain_electrode'].predict(X_test_new.values)
import matplotlib.pyplot as plt
plt.figure(figsize=(12,6))
plt.plot(X_test_new.index, X_test_new.iloc[:,0], label='electrode')
plt.plot(X_test_new.index, Y_test_new, label='dataglove (GT)')
plt.plot(X_test_new.index, Y_pred, label='dataglove (PRED)')

plt.legend()
plt.show()
# Export X_test_new, Y_test_new, and Y_pred to an Excel file
export_df = pd.DataFrame({'X_test_new': X_test_new.iloc[:, 0], 'Y_test_new':
Y_test_new.squeeze(), 'Y_pred': Y_pred.squeeze()})
export_df.to_excel('predictions_MLP.xlsx', index=False)
```

References

1. H. Song, T. Kim, S. Kang, H. Jin, K. Lee and H. J. Yoon, *Small*, 2020, **16**, 1903391.
2. N. J. Morris, Z. J. Farrell and C. E. Tabor, *Nanoscale*, 2019, **11**, 17308-17318.
3. G. Falkovich, *Fluid mechanics: A short course for physicists*, Cambridge University Press, 2011.
4. H. Schlichting and K. Gersten, *Boundary-layer theory*, springer, 2016.
5. J. P. Holman, *Heat transfer*, McGraw Hill, 1986.
6. M. J. Ford, D. K. Patel, C. Pan, S. Bergbreiter and C. Majidi, *Adv Mater*, 2020, **32**, e2002929.
7. S.-Y. Fu, X.-Q. Feng, B. Lauke and Y.-W. Mai, *Composites Part B: Engineering*, 2008, **39**, 933-961.
8. T. R. Lear, S.-H. Hyun, J. W. Boley, E. L. White, D. H. Thompson and R. K. Kramer, *Extreme Mechanics Letters*, 2017, **13**, 126-134.
9. H.-J. Sheen, B. Panigrahi, T.-R. Kuo, W.-C. Hsu, P.-S. Chung, Q.-Z. Xie, C.-Y. Lin, Y.-S. Chang, C.-T. Lin and Y.-J. Fan, *Biosensors and Bioelectronics*, 2022, **210**, 114338.
10. L. W. Taylor, S. M. Williams, J. S. Yan, O. S. Dewey, F. Vitale and M. Pasquali, *Nano Letters*, 2021, **21**, 7093-7099.
11. B. Sun, R. N. McCay, S. Goswami, Y. Xu, C. Zhang, Y. Ling, J. Lin and Z. Yan, *Advanced Materials*, 2018, **30**, 1804327.
12. W. Tang, Y. Zhou, S. Chen, S. Yu, Y. Yang, J. Lin, S. Yin, Y. Ma and B. Hu, *ACS Materials Letters*, 2021, **3**, 1385-1393.
13. Y.-T. Kwon, Y.-S. Kim, S. Kwon, M. Mahmood, H.-R. Lim, S.-W. Park, S.-O. Kang, J. J. Choi, R. Herbert, Y. C. Jang, Y.-H. Choa and W.-H. Yeo, *Nature Communications*, 2020, **11**, 3450.
14. R. A. Nawrocki, H. Jin, S. Lee, T. Yokota, M. Sekino and T. Someya, *Advanced Functional Materials*, 2018, **28**, 1803279.
15. S. Guler, A. Golparvar, O. Ozturk and M. K. Yapici, *IEEE Sensors Letters*, 2022, **6**, 1-4.
16. J. Huang, A. Chen, S. Han, Q. Wu, J. Zhu, J. Zhang, Y. Chen, J. Liu and L. Guan, *Advanced Science*, 2023, **10**, 2301116.
17. W. B. Han, G.-J. Ko, K.-G. Lee, D. Kim, J. H. Lee, S. M. Yang, D.-J. Kim, J.-W. Shin, T.-M. Jang, S. Han, H. Zhou, H. Kang, J. H. Lim, K. Rajaram, H. Cheng, Y.-D. Park, S. H. Kim and S.-W. Hwang, *Nature Communications*, 2023, **14**, 2263.
18. H. Huang, J. Shen, S. Wan, L. Han, G. Dou and L. Sun, *ACS Applied Materials & Interfaces*, 2023, **15**, 11549-11562.
19. B. B. Etana, B. Malengier, T. Kwa, J. Krishnamoorthy and L. V. Langenhove, *Sensors*, 2023, **23**.
20. M. Colachis, B. R. Schlink, S. Colachis, K. Shqau, B. L. Huegen, K. Palmer and A. Heintz, *Sensors*, 2024, **24**.
21. S. Yao, W. Zhou, R. Hinson, P. Dong, S. Wu, J. Ives, X. Hu, H. Huang and Y. Zhu, *Advanced Materials Technologies*, 2022, **7**, 2101637.
22. X. Wang, W. Qiu, C. Lu, Z. Jiang, C. Hou, Y. Li, Y. Wang, H. Du, J. Zhou and X. Y. Liu, *Advanced Functional Materials*, 2024, **34**, 2311535.
23. Y. Jiang, S. Ji, J. Sun, J. Huang, Y. Li, G. Zou, T. Salim, C. Wang, W. Li, H. Jin, J. Xu, S. Wang, T. Lei, X. Yan, W. Y. X. Peh, S.-C. Yen, Z. Liu, M. Yu, H. Zhao, Z. Lu, G. Li, H. Gao, Z. Liu, Z. Bao and X. Chen, *Nature*, 2023, **614**, 456-462.
24. H. Jiang, J. Zhang, M. Qin, J. Zhang, X. Zou and X. Weng, *Sensors and Actuators A: Physical*, 2023, **356**, 114359.

25. J. Lee, S. Shin, S. Lee, J. Song, S. Kang, H. Han, S. Kim, S. Kim, J. Seo, D. Kim and T. Lee, *ACS nano*, 2018, **12**, 4259-4268.
26. H. Jin, M. O. G. Nayeem, S. Lee, N. Matsuhisa, D. Inoue, T. Yokota, D. Hashizume and T. Someya, *ACS nano*, 2019, **13**, 7905-7912.
27. S. Yao, J. Yang, F. R. Poblete, X. Hu and Y. Zhu, *ACS Applied Materials & Interfaces*, 2019, **11**, 31028-31037.
28. W. Wang, Y. Liu, M. Ding, T. Xia, Q. Gong, X. Zeng, Z. Cai and Y. Hu, *Nano Energy*, 2023, **116**, 108832.
29. S. Ko, A. Chhetry, D. Kim, H. Yoon and J. Y. Park, *ACS Applied Materials & Interfaces*, 2022, **14**, 31363-31372.
30. A. Chen, J. Zhang, J. Zhu, Z. Yan, Q. Wu, S. Han, J. Huang and L. Guan, *Journal of Materials Chemistry A*, 2023, **11**, 4977-4986.
31. M. Lan, J. Zhang, J. Zhou and H. Gu, *ACS Applied Materials & Interfaces*, 2024, **16**, 23838-23854.
32. J. Liang, K. Ma, W. Gao, Y. Xin, S. Chen, W. Qiu, G. Shen and X. He, *Sensors & Diagnostics*, 2024, **3**, 256-268.
33. B. Polat, T. Rafeedi, L. Becerra, A. X. Chen, K. Chiang, V. Kaipu, R. Blau, P. P. Mercier, C.-K. Cheng and D. J. Lipomi, *Advanced Sensor Research*, 2023, **2**, 2200060.
34. Y. Zhao, D. Gan, L. Wang, S. Wang, W. Wang, Q. Wang, J. Shao and X. Dong, *Advanced Materials Technologies*, 2023, **8**, 2201566.
35. Y. Zhao, Y. Ohm, J. Liao, Y. Luo, H.-Y. Cheng, P. Won, P. Roberts, M. R. Carneiro, M. F. Islam, J. H. Ahn, L. M. Walker and C. Majidi, *Nature Electronics*, 2023, **6**, 206-215.